International Journal of Heat and Fluid Flow 116 (2025) 109888

Contents lists available at ScienceDirect

International Journal of Heat and Fluid Flow

journal homepage: www.elsevier.com/locate/ijhff

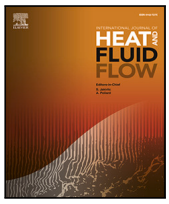

Characterization of hydrodynamic and thermal properties of anisotropic irregular roughness

Jiasheng Yang [a], Alexander Stroh [a,*], Shervin Bagheri [b], Bettina Frohnapfel [a], Pourya Forooghi [c]

[a] Institute of Fluid Mechanics, Karlsruhe Institute of Technology, Kaiserstr.10, Karlsruhe, 76131, Germany
[b] FLOW, Dept. Engineering Mechanics, Royal Institute of Technology (KTH), Brinellvägen 8, Stockholm, SE-100 44, Sweden
[c] Department of Mechanical & Production Engineering, Aarhus University, Katrinebjergvej 89G-F, Aarhus, 8200, Denmark

ARTICLE INFO

Keywords:
Anisotropic roughness
Ice accretion
Direct numerical simulation

ABSTRACT

Rough surfaces are prevalent in flow-related applications due to surface degradation. The roughness topography can alter the surface skin friction and heat transfer in turbulent flows. Depending on the different mechanism of the roughness formation process, the roughness topography may exhibit anisotropic properties. The present work aims to shed light on the effect of roughness anisotropy on skin friction and heat transfer by systematically varying roughness properties in different directions and across various scales. To this end, irregular anisotropic rough surfaces are generated based on 2-D power spectrum (PS). The surfaces are generated with Gaussian height probability density functions (PDF) and with either matched surface anisotropy ratios (SAR=L_x^{Corr}/L_z^{Corr}) or effective slope ratios (ESR=ES_x/ES_z). By adjusting the 2-D PS, the degree of anisotropy is varied at different wavenumbers, some surfaces are more anisotropic at large scales andsome at small scales. Direct numerical simulations are performed to study turbulent flow over these anisotropic rough surfaces at $\mathrm{Re}_\tau = 500$, $Pr = 0.71$. The results demonstrate that the roughness anisotropy play a pivotal role in influencing both skin friction and heat transfer of the rough surface, leading to alterations of up to more than 50% in the roughness function ΔU^+ and the temperature roughness function $\Delta\Theta^+$. Detailed analysis indicates that commonly used parameters, SAR or ESR alone, may not be the most appropriate predictive quantities to characterize the effects of anisotropic irregular roughness. In light of this, we introduce a new roughness topographical parameter η_{SA}= ESR/SAR that successfully correlates with the observed anisotropic effect. The suitability of this new parameter is assessed through comprehensive analysis of both the current dataset and the anisotropic roughness from literature.

1. Introduction

Hydraulically rough surfaces are frequently observed in flow-related applications. Predicting roughness-induced skin friction is of crucial economic and environmental significance, especially for the transportation industry (Holm M. P. Schultz et al., 2011; Chung et al., 2021). Development of a universally applicable predictive correlation for the impact of roughness remains a challenge due to the inherent multi-scale and stochastic nature of roughness. Over the past few decades, significant endeavors have been devoted to the characterization of roughness drag solely based on their topographical properties (see e.g. Flack et al. (2016), Flack (2018), Schultz and Flack (2007, 2009), Thakkar et al. (2017) and Ramani et al. (2024)). These trace back to the work of Nikuradse (1933), who demonstrated a correlation between the height of uniform sand grains and their skin friction coefficient (C_f). The skin friction coefficient is defined as

$$C_f = \frac{2\tau_w}{\rho U_b^2} = \frac{2}{U_b^{+2}}, \tag{1}$$

where τ_w represents wall shear stress, $U_b = \int_0^{2\mathrm{H}} U\,dy/(2\mathrm{H} - 2k_{\mathrm{md}})$ is the bulk velocity with U denoting extrinsically averaged (i.e. including solid domain parts into the time–space average) velocity. H represents the channel half height measured from the deepest trough and $k_{\mathrm{md}} = \int_S k\mathrm{d}S$ is the averaged roughness height measured from the deepest trough, where S is the projected area of rough surface. The y-coordinate is measured from the bottom of the roughness. The rough surfaces are also responsible for altering heat transfer across the domain. Temperature is treated as a passive scalar, indicating forced convection with negligible buoyancy. The wall temperature is held constant at zero, consistent with prior forced convection studies over rough surfaces,

* Corresponding author.
E-mail address: alexander.stroh@kit.edu (A. Stroh).

https://doi.org/10.1016/j.ijheatfluidflow.2025.109888
Received 14 January 2025; Received in revised form 4 April 2025; Accepted 7 May 2025
Available online 5 June 2025

e.g., MacDonald et al. (2019). The heat transfer rate can be quantified by the Stanton number St analogous to C_f, which is defined as:

$$St = \frac{1}{U_b^+ \Theta_b^+}, \tag{2}$$

where $\Theta_b = \int_0^{2H} U\Theta \mathrm{d}y / \int_0^{2H} U \mathrm{d}y$. According to Townsend's outer layer similarity hypothesis (Townsend, 1976), the turbulence in the outer layer remains unaffected by the perturbations exerted by near-wall roughness. As a consequence the impact of the roughness on the outer layer flow manifests merely in the downward shift of the mean velocity profile. This offset in the logarithmic layer is anticipated to be constant in the outer layer and is denoted as the (Hama) roughness function ΔU^+ (Hama, 1954). The logarithmic law in the context of surface roughness is thus given by:

$$U^+ = \frac{1}{\kappa} \ln y^+ + B - \Delta U^+, \tag{3}$$

here $\kappa \approx 0.41$ denotes the von Kármán constant and $B = 5.2$ is the intersect of the log-law. Based on the outer layer similarity hypothesis and the assumption of negligible deviation of viscous and buffer layer velocity profile from the idealized velocity profile, the skin friction coefficient of the rough surface ($C_{f,r}$) can be used to estimate ΔU^+ via

$$\Delta U^+ = \sqrt{\frac{2}{C_{f,s}}} - \sqrt{\frac{2}{C_{f,r}}}. \tag{4}$$

Here, $C_{f,s}$ represents skin friction of smooth surface at identical friction Reynolds number Re_τ. The outer-layer similarity of the temperature profile is also observed in the literature (Kader, 1981; Kawamura et al., 1999; Yaglom, 1979), which leads to the logarithmic law of temperature:

$$\Theta^+ = \frac{1}{\kappa_\theta} \ln y^+ + A_0 - \Delta\Theta^+, \tag{5}$$

where $\kappa_\theta \approx 0.47$, A_0 is a function of Pr and $\Delta\Theta^+$ is the temperature roughness function.

A substantial body of research has been dedicated to developing universally applicable methods for predicting skin friction based solely on surface topographical properties (Chung et al., 2021). These predictions typically rely on either mathematical empirical correlations (e.g. in Flack and Schultz (2010), Chan et al. (2015) and Forooghi et al. (2017)) or machine learning models (e.g. in Jouybari et al. (2021), Sanhueza et al. (2023) and Yang et al. (2023a)). Similarly, significant attention has been given to studying heat transfer across rough surfaces (Peeters and Sandham, 2019; MacDonald et al., 2019; Garg et al., 2024). However, due to its dependence on Reynolds and Prandtl numbers, heat transfer predictions require exploration over a larger parameter space. While these studies have covered various types of roughness, it is noteworthy that most of this research assumes rough surface isotropy. This assumption implies that statistical metrics of the rough surface remain consistent in all wall-parallel directions, leading to the expectation that the effects of roughness – despite the stochastic nature of irregular rough surfaces – are invariant with respect to the wall-parallel flow orientation. In practical applications, perfectly isotropic rough surfaces barely exist, as nearly all rough surfaces exhibit some degree of anisotropy. This introduces uncertainty when applying models based on isotropic assumptions to predict flow behavior. For instance, rough surfaces on aircraft (Yang et al., 2023b) or turbine blades (Barros et al., 2018) often display directional characteristics that can significantly impact thermal and hydrodynamic performance. To address this challenge, the present work aims to reduce the uncertainty associated with surface anisotropy by incorporating its influence on skin friction and heat transfer.

In the study conducted by Jelly et al. (2022), surface anisotropy in artificial rough surfaces was introduced by independently varying the characteristic lengths of exponential roughness height correlation functions in the streamwise and spanwise directions. It is demonstrated that the influence of anisotropic roughness on turbulent flow exhibits significant variation depending on the directional alignment of the roughness structures. To quantify surface anisotropy, the effective slope ratio $\mathrm{ESR} = \mathrm{ES}_x/\mathrm{ES}_z$ is employed, where $\mathrm{ES}_{x,z}$ represent effective slopes in the streamwise and spanwise directions, respectively:

$$\mathrm{ES}_x = \left\langle \frac{\partial k}{\partial x} \right\rangle \quad \text{and} \quad \mathrm{ES}_z = \left\langle \frac{\partial k}{\partial z} \right\rangle, \tag{6}$$

where k represents the roughness height map as a function of the wall-parallel coordinates x and z, and $\langle\varphi\rangle = \frac{1}{S}\int_S \varphi \mathrm{d}S$ denotes the spatial average of an arbitrary quantity φ over the x-z plane. Alternatively, Busse and Jelly (2020) used the ratio of correlation lengths in wall-parallel directions $\mathrm{SAR} = L_x^{Corr}/L_z^{Corr}$ for representing roughness anisotropy. The correlation length L^{Corr} is defined as the length-scale at which the auto-correlation of roughness distribution decreases to 0.2 (Thakkar et al., 2017). Nevertheless, as will be demonstrated in the present work, characterizing the current set of anisotropic roughness using each of these parameters leads to noticeable data scatter, suggesting a incomplete representation of the surface anisotropy.

Many studies have shown that secondary motions – coherent cross-sectional flows with alternating high- and low-momentum regions – emerge over rough surfaces in various configurations. Busse et al. (2017) report the presence of secondary motion directly above the irregular roughness surface and study their Reynolds-number dependence. Barros and Christensen (2014) observed persistent secondary flows over complex turbine-blade roughness, linked to spanwise height gradients, with increased Reynolds stresses and TKE extending into the outer layer. Womack et al. (2022) confirmed similar structures over randomly arranged cones, correlated with roughness front edges. Kaminaris et al. (2023) found stronger secondary flows in random roughness via DNS, driven by vortex stretching at roughness leading edges. Although not focused on secondary flows, Medjnoun et al. (2023) highlighted how roughness complexity affects drag predictions, underscoring the need to capture such flow structures. Together, these works show that large-scale secondary motions arise not only from structured roughness (Vanderwel et al., 2019; Stroh et al., 2020a) but also from random, anisotropic surfaces (Stroh et al., 2020b), framing the context for this study.

In the present work, a comprehensive numerical investigation on the drag and heat transfer of a set of anisotropic rough surfaces is performed on roughness geometries exhibiting different degrees of anisotropy across multiple length scales. To this end, a two-dimensional anisotropic power spectral (PS) representation is employed to construct a roughness database with systematically varied anisotropy parameters. These anisotropic rough surfaces are subsequently investigated through direct numerical simulations (DNS) at $\mathrm{Re}_\tau = 500$ and $Pr = 0.71$. Finally, a new roughness parameter $\eta_{\mathrm{SA}} = \mathrm{ESR}/\mathrm{SAR}$ is proposed to characterize the impact of surface anisotropy on the alteration in drag and heat transfer. Correlation functions describing the alterations in drag and heat transfer due to roughness anisotropy are derived by fitting the present dataset and subsequently validated against roughness data from the literature.

2. Methodology

2.1. Anisotropic roughness generation

In the present work, artificial irregular rough surfaces are generated through a mathematical random roughness generation method where the PS and PDF of the roughness can be prescribed (Pérez-Ràfols and Almqvist, 2019). The applicability of this generation method for generating isotropic realistic surface surrogates based on 1-D PS profile is demonstrated in our previous publication (Yang et al., 2023b). The roughness structures are represented by 2-D discrete elevation maps as functions of wall-parallel coordinates $k(x, z)$. In the current database, the characteristic roughness height is represented by the 99% confidence interval of the roughness height PDF, k_{99}. We prescribe

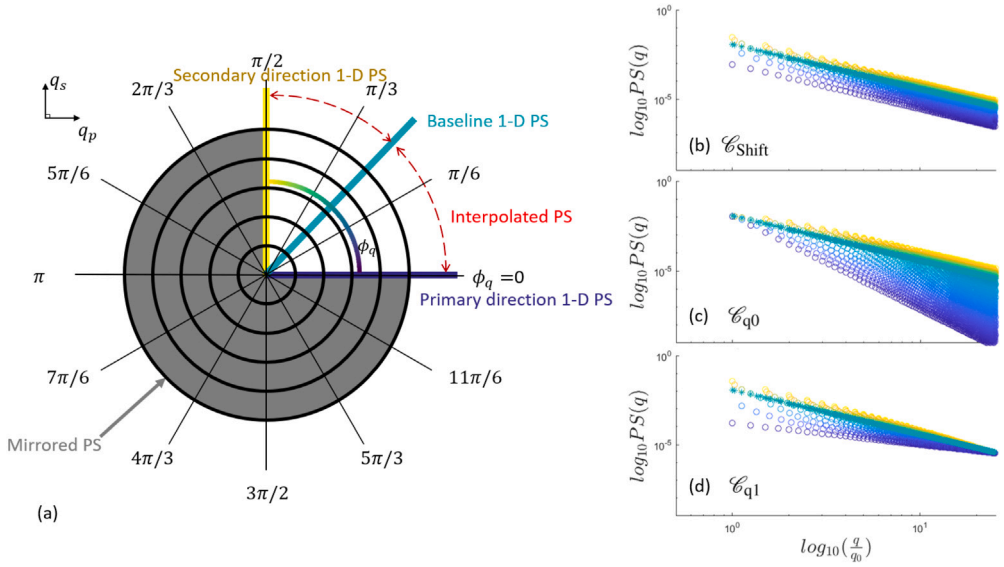

Fig. 1. (a): illustration of 2-D PS generation methodology. (b–d): illustrations of 2-D PS as functions of $q = \sqrt{q_p^2 + q_s^2}$ for $\mathscr{C}_{\text{Shift}}$, $\mathscr{C}_{\text{q0}}$ and $\mathscr{C}_{\text{q1}}$, respectively. Color indicates ϕ_q, Asterisks represent the baseline 1-D PS profile. (For interpretation of the references to color in this figure legend, the reader is referred to the web version of this article.)

Table 1
Statistics of investigated roughness along with their simulation results. ESR = ES_x/ES_z denotes the ratio of streamwise and spanwise effective slopes. The shaded blocks indicate the values that are kept consistent across different cases.

Case		SAR	ESR	ES_x	ES_z	L_x^{Corr}/H	L_z^{Corr}/H	ΔU^+	$\Delta\Theta^+$	$C_f \times 100$	$St \times 100$	$\left(\frac{\sqrt{V^2+W^2}}{U_b}\right)_{max}$ [%]
Isotropic	$\mathscr{C}_{\text{Ref}}$	1.0	1.0	0.24	0.24	0.31	0.30	5.53	2.14	1.30	0.66	2.3
Streamwise	$\mathscr{C}^{\text{SAR}}_{\text{Shift},x}$	3.10	0.55	0.16	0.29	0.65	0.21	4.22	1.53	1.07	0.57	2.1
	$\mathscr{C}^{\text{SAR}}_{\text{q0},x}$	3.00	0.44	0.14	0.32	0.45	0.15	4.09	1.52	1.05	0.57	2.9
	$\mathscr{C}^{\text{SAR}}_{\text{q1},x}$	3.23	0.77	0.20	0.26	0.71	0.22	4.47	1.66	1.11	0.59	1.8
	$\mathscr{C}^{\text{ESR}}_{\text{Shift},x}$	1.56	0.77	0.20	0.26	0.39	0.25	5.00	1.88	1.20	0.62	2.3
	$\mathscr{C}^{\text{ESR}}_{\text{q0},x}$	1.10	0.77	0.20	0.27	0.32	0.29	5.15	1.88	1.23	0.64	2.6
Spanwise	$\mathscr{C}^{\text{SAR}}_{\text{Shift},z}$	0.33	1.88	0.30	0.16	0.20	0.61	6.42	2.39	1.52	0.74	3.2
	$\mathscr{C}^{\text{SAR}}_{\text{q0},z}$	0.34	2.29	0.32	0.14	0.15	0.44	6.40	2.37	1.51	0.73	3.3
	$\mathscr{C}^{\text{SAR}}_{\text{q1},z}$	0.31	1.30	0.26	0.20	0.20	0.64	6.07	2.28	1.43	0.70	3.2
	$\mathscr{C}^{\text{ESR}}_{\text{Shift},z}$	0.66	1.27	0.26	0.21	0.25	0.38	5.95	2.17	1.40	0.69	3.5
	$\mathscr{C}^{\text{ESR}}_{\text{q0},z}$	0.88	1.30	0.26	0.20	0.28	0.32	5.85	2.24	1.38	0.69	3.5

$k_{99} = 0.1$H for the considered roughness, where H indicates the channel half height. Consistent with the previous publication utilizing the same generation algorithm (Yang et al., 2022), extreme roughness peaks or valleys are truncated beyond $1.2 \times k_{99}$ around k_{md}, where $k_{md} = \int_S k\mathrm{d}S/S$ denotes the roughness melt-down height measured from the lowest roughness valley.

Initially, the reference isotropic roughness $\mathscr{C}_{\text{Ref}}$ is introduced based on the baseline 1-D power-law PS: $E_k(q) = C_0(\|q\|/q_0)^p$ where q is the wavenumber, $q_0 = 2\pi/\lambda_0$ is the smallest wavenumber corresponding to the largest in-plane roughness length scale $\lambda_0 = 2$H, C_0 is a constant to scale the roughness height, and $p = 2.5$ is the slope of PS. Following this definition, anisotropic 2-D PS are constructed. First of all, the primary and secondary directions – perpendicular to each other – are defined on the 2-D PS map with coordinate q_p and q_s, respectively. The angular coordinate is calculated by $\phi_q = \tan^{-1}(q_s/q_p)$. The baseline 1-D PS profile is assigned to $\phi_q = \pi/4$. Subsequently, to achieve different anisotropic behavior, three types of PS profile adjustments in the primary direction – i.e. along $\phi_q = 0$ – are employed and denoted with the corresponding abbreviations:

1. $\mathscr{C}_{\text{Shift}}$: shifting the baseline PS profile
2. $\mathscr{C}_{q0}$: adjusting PS slope p while maintaining identical PS at lowest in-plane roughness wavenumber q_0
3. $\mathscr{C}_{q1}$: adjusting PS slope p while maintaining identical PS at highest in-plane roughness wavenumber q_1

Here the primary direction $\phi_q = 0$ can be placed either in streamwise direction (denoted with subscript x) or spanwise direction (denoted with subscript z) to generate differently oriented anisotropic roughness. On the other hand, the PS in the secondary direction, $\phi_q = \pi/2$, is determined accordingly to ensure that the resulting azimuthally averaged 2-D PS matches the baseline 1-D PS profile. Based on that, the first quarter of the 2-D PS – i.e. within $\phi_q = [0, \pi/2]$ – is constructed through azimuthal interpolation based on the three pre-defined 1-D profiles on $\phi_q = 0$, $\phi_q = \pi/4$ and $\phi_q = \pi/2$. The rest part of the 2-D PS map, i.e. $\phi_q \in]\pi/2, 2\pi[$ is obtained by mirroring the known quarter of the PS. An illustration of the three aforementioned types of 2-D anisotropic PS is depicted in Fig. 1. The present roughness generation approach produces structures that are elongated along the primary wavenumber q_p. Consequently, whether the roughness is streamwise- or spanwise-aligned depends on the orientation of q_p relative to the flow direction. Specifically, when q_p is aligned with the streamwise direction, the roughness can be considered streamwise-aligned, and conversely, when q_p is oriented in the spanwise direction, the roughness is spanwise-aligned. The exemplary roughness corresponding to each considered roughness case are depicted in Fig. 2. As can be seen, the generated roughness exhibits distinct characteristics at both large and small scales, depending on the configuration of PS. The exemplary large- and small-scale structures are marked with solid and dashed lines, respectively. While the reference roughness demonstrates isotropic structures across all scales, different types

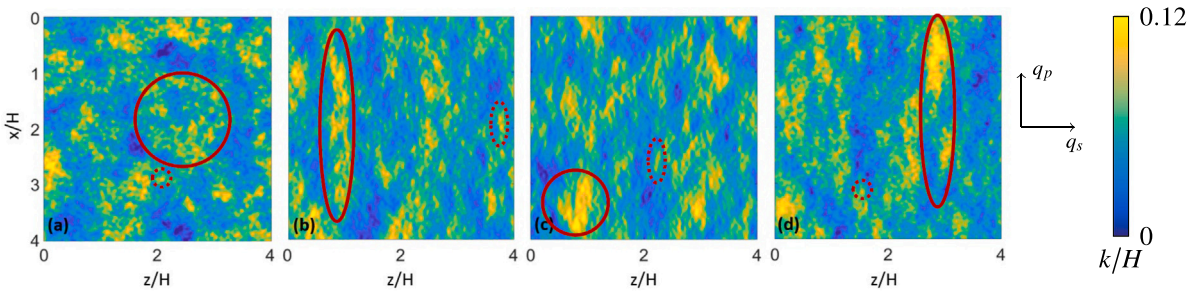

Fig. 2. Exemplary roughness height distribution for different types of surface anisotropy, (a) $\mathscr{C}_{\mathrm{Ref}}$ (isotropic reference), (b) $\mathscr{C}_{\mathrm{Shift}}$, (c) $\mathscr{C}_{\mathrm{q1}}$ and (d) $\mathscr{C}_{\mathrm{q0}}$. The large- and small-scale structures are marked with solid and dashed lines, respectively. Please note that the flow direction is either along q_s or q_p among the considered cases.

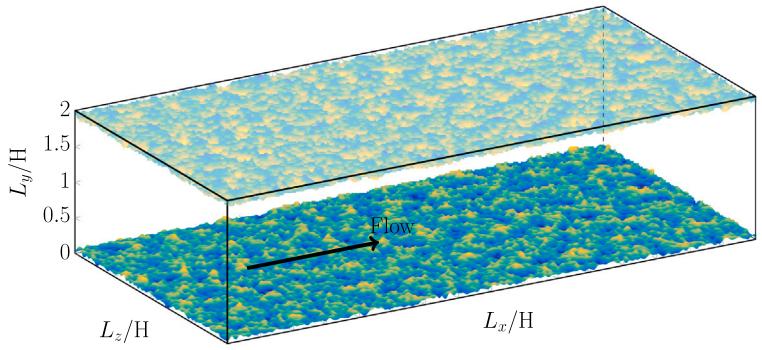

Fig. 3. Schematic representation of simulation domain with an exemplary rough surface mounted on the channel walls.

of anisotropy exhibit varying properties. Specifically, $\mathscr{C}_{\mathrm{Shift}}$ contains anisotropic features at both large and small scales. In contrast, the roughness structure of $\mathscr{C}_{\mathrm{q1}}$ gradually transitions toward isotropy as the length scale increases. Conversely, $\mathscr{C}_{\mathrm{q0}}$ exhibits anisotropic large-scale structures, whereas small-scale structures remain isotropic.

Two groups of surfaces are studied to investigate the effects of anisotropic roughness: one with matched surface anisotropy ratios (SAR) and the other with matched effective slope ratios (ESR). For the SAR group, cases with SAR ≈ 3 (or the reversed values for spanwise-oriented cases) are consistently maintained, denoted by the superscript SAR. Within this group, the PS slope p associated with q_p is set to 1.2 for $\mathscr{C}^{\mathrm{SAR}}_{\mathrm{q1}}$ and 5.2 for $\mathscr{C}^{\mathrm{SAR}}_{\mathrm{q0}}$, respectively. In the ESR group, the controlled parameter shifts to the ratio of effective slopes in the streamwise and spanwise directions. By adjusting the PS of $\mathscr{C}_{\mathrm{Shift}}$ and $\mathscr{C}_{\mathrm{q0}}$, surfaces are designed to achieve the same ESR values as those in the $\mathscr{C}^{\mathrm{SAR}}_{\mathrm{q1}}$ group. These cases are labeled with the superscript ESR.In this group, the PS slope p associated with q_p is selected to be 2.8 for $\mathscr{C}^{\mathrm{ESR}}_{\mathrm{q0}}$. The resulting roughness statistics are illustrated in Table 1. Based on the values presented in Table 1 and the corresponding PS slope p for the anisotropic cases, it can be concluded that the anisotropy metrics employed in this study capture distinct aspects of surface anisotropy. Specifically, ESR predominantly characterizes small-scale roughness variations, whereas SAR describes the structural relationships at larger scales. Thus, ESR and SAR serve as indicators of surface anisotropy at different length scales. For example, a surface with an ESR value significantly deviating from unity but an SAR value close to unity suggests the presence of anisotropic small-scale roughness while maintaining isotropic large-scale structures, and *vice versa*.

2.2. Direct numerical simulation

Direct Numerical Simulations (DNS) are carried out in fully developed turbulent channels driven by constant pressure gradient (CPG) with the spectral solver SIMSON (Chevalier et al., 2007). SIMSON is a spectral solver, where Fourier expansions are employed in the periodic directions, while Chebyshev polynomials are used in the wall-normal direction. Time integration is performed using an explicit third-order Runge–Kutta scheme for convective terms and a second-order implicit Crank–Nicolson scheme for viscous terms. The initial velocity field is generated using built-in functionality in SIMSON, which can generate a basic laminar flow superimposed with various disturbances, such as localized disturbances, waves, and random noise (Chevalier et al., 2007). Within the channel, identical roughness patches are installed on both upper and lower wall as illustrated in Fig. 3. The roughness with no-slip boundary and zero-temperature boundary conditions are realized by imposing immersed boundary method (IBM) following Goldstein et al. (1993) Therefore, the incompressible Navier–Stokes equations and the balance equation for the passive scalar Θ is formulated as:

$$\boldsymbol{\nabla}\cdot\mathbf{u} = 0, \tag{7}$$

$$\frac{\partial \mathbf{u}}{\partial t} + \boldsymbol{\nabla}\cdot(\mathbf{u}\mathbf{u}) = -\frac{1}{\rho}\boldsymbol{\nabla}p + \nu\nabla^2\mathbf{u} - \frac{1}{\rho}P_x\boldsymbol{e}_x + \mathbf{f}_{\mathrm{IBM}}, \tag{8}$$

$$\frac{\partial \theta}{\partial t} + \nabla\cdot(\mathbf{u}\theta) = \alpha\nabla^2\theta + Q + \mathbf{f}_{\theta}, \tag{9}$$

where p and e_x represent pressure fluctuations and the streamwise base vector, respectively. All fluid properties, namely density ρ, kinematic viscosity ν and thermal diffusivity α are assumed to be constant. Possible temperature changes due to viscous diffusion are not included. The grid resolution in the present study is chosen to ensure that the smallest prescribed roughness wavelength is resolved with at least eight grid points. This resolution has been thoroughly evaluated in previous studies conducted by the authors (Yang et al., 2022, 2021). A mesh-independence analysis was performed to confirm the adequacy of the resolution for capturing the finest-scale roughness structures. The currently employed solver and IBM methodology have been further validated by comparing simulation results obtained from different solvers utilizing both body-conforming and immersed boundary roughness modeling approaches (Theobald et al., 2021) and a successful comparison to experimental data (Frohnapfel et al., 2024). External source terms for momentum and temperature are added in the equation, denoted as $\mathbf{f}_{\mathrm{IBM}}$ and $\mathbf{f}_{\Theta}$, respectively. Periodic boundary condition

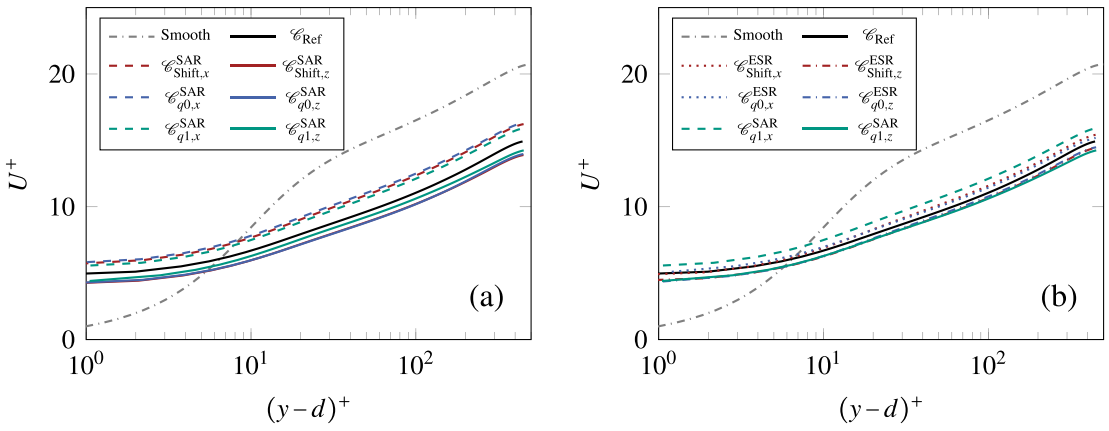

Fig. 4. DNS results of considered cases. The color indicates different types of roughness anisotropy. The inner-scaled mean velocity profiles are compared among the cases with same (a) SAR and (b) ESR.

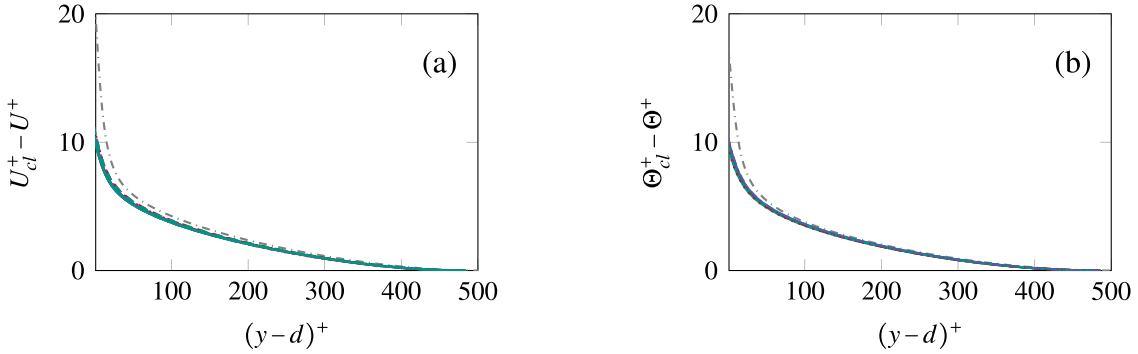

Fig. 5. Mean velocity (a) and temperature (b) deficit profiles, line styles correspond to Fig. 4. U^+_{cl} and Θ^+_{cl} are the inner-scaled mean center line velocity and temperature, respectively.

is applied in streamwise and spanwise directions. P_x indicates the constant pressure gradient in the flow direction. The value of P_x is predefined to achieve $\mathrm{Re}_\tau = u_\tau \mathrm{H}_{\mathrm{eff}}/\nu = 500$. Here $u_\tau = \sqrt{\tau_w/\rho}$ denotes friction velocity, $\tau_w = P_x \mathrm{H}_{\mathrm{eff}}$ is the wall shear stress corresponding to the effective channel height $\mathrm{H}_{\mathrm{eff}} = \mathrm{H} - k_{md}$. The term $Q = -u\mathrm{d}\Theta/\mathrm{d}x$ represents the temperature source in order to achieve a stationary state of the temperature field. The velocity and temperature distribution (Raupach, 1992) is double-averaged in wall-parallel directions and time and denoted as $\langle\overline{u}\rangle = U(y)$ and $\langle\overline{\theta}\rangle = \Theta(y)$, respectively. In the considered system, the hot fluid is being cooled by the walls as it flows through the domain. In a statistically steady, fully developed flow, where the time-averaged bulk temperature remains constant, the heat added via this body source term balances the heat lost through the walls. This approach is similar to the method proposed by Kasagi et al. (1992), where a dynamically adjusted source term is employed to regulate the temperature field. The dimension of the DNS domain is $(L_x, L_y, L_z) = (8\mathrm{H}, 2\mathrm{H}, 4\mathrm{H})$, with grid resolution of $(N_x, N_y, N_z) = (900, 401, 480)$. The domain can accommodate four of the largest roughness wavelengths, $\lambda_0 = 2H$, in the streamwise direction and two in the spanwise direction. The statistical analysis of the turbulent flow is conducted after an initial running-in period of approximately 40 Flow-Through-Times (FTT), where FTT= TU_b/L_x, T represents total simulation time. The flow statistic data are collected over a time span ranging from 50 to 150 FTT.

3. Results

3.1. Impact of anisotropic roughness on skin friction

The inner-scaled mean velocity profiles U^+ are illustrated in Fig. 4 as functions of $(y-d)^+$, grouped by the shared roughness parameters. Here the virtual origin of the rough wall is determined by the zero-plane displacement d following Jackson's definition (Jackson, 1981). Moreover, we include $\mathscr{C}_{\mathrm{Ref}}$ in the figures with the solid black line. The notable offset observed in U^+ relative to $\mathscr{C}_{\mathrm{Ref}}$ correspond to a discrepancy in the calculated ΔU^+ of up to more than ± 1 in viscous unit. This level of uncertainty highlights the critical importance of incorporating surface anisotropy into the characterization of arbitrary irregular roughness. Additionally, the deficit mean profiles (velocity and temperature profiles) are depicted in Fig. 5. The different rough surfaces reveal a high similarity in this representation with distinct deviations from the smooth wall reference. These deviations indicate the presence of a large roughness sublayer which was previously related to the formation of secondary flow over rough surfaces with large spanwise wavelength in their surface properties (Jelly et al., 2022). The secondary flow that develops for the present surfaces is discussed in Section 3.3 of the present manuscript.

The C_f as well as the ΔU^+ values are computed for each case and are shown in Table 1. The ΔU^+ values are plotted in Fig. 6(a) against SAR. In the figure, different types of roughness anisotropy are distinguished by symbol color, the baseline isotropic case is included with black circle. Similarly to the previous observations, the variation of ΔU^+ is evident between streamwise and spanwise aligned roughness. Generally, the ΔU^+ values decrease with SAR. The impact of surface anisotropy of different types is obvious, yet to distinguishable extent. The variation of ΔU^+ of the streamwise anisotropic roughness (SAR > 1) can be clearly observed. The $\mathscr{C}^{\mathrm{SAR}}_{\mathrm{q0},x}$ and $\mathscr{C}^{\mathrm{ESR}}_{\mathrm{q0},x}$ cases demonstrate the most significant decrease in ΔU^+ with increasing SAR, while $\mathscr{C}^{\mathrm{SAR}}_{\mathrm{q1},x}$ achieves the least decrease in ΔU^+ under similar SAR condition. In the cases of spanwise anisotropy (SAR < 1), a similar conclusion can be drawn, whereby ΔU^+ exhibits lowest sensitivity to SAR for $\mathscr{C}^{\mathrm{SAR}}_{\mathrm{q1},z}$. However, the increase

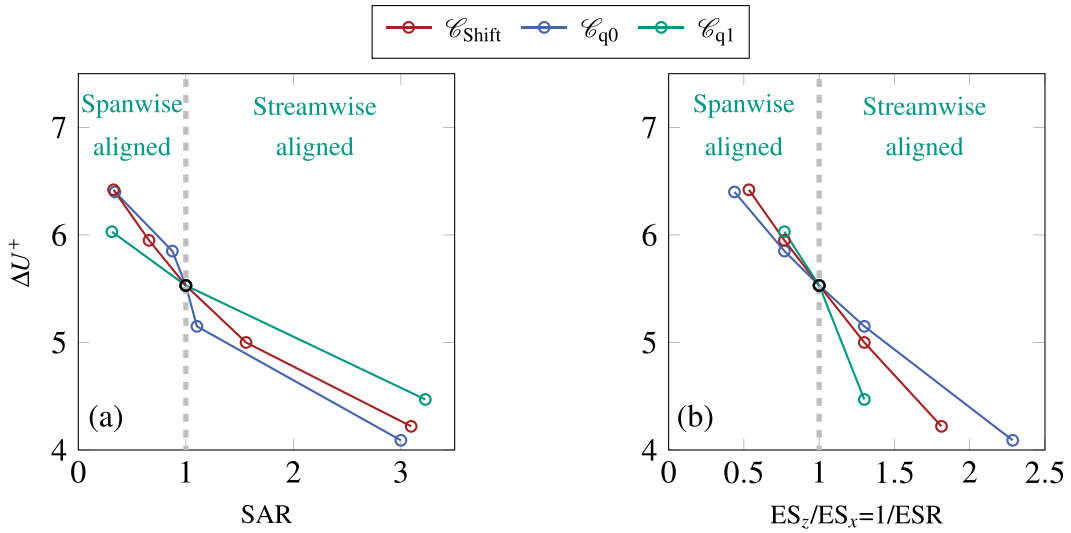

Fig. 6. The roughness function, ΔU^+, plotted as functions of the (a) SAR, (b) ES_z/ES_x = 1/ESR. The color indicates different types of roughness anisotropy. The reference case $\mathscr{C}_{\text{Ref}}$ is represented by black circle.

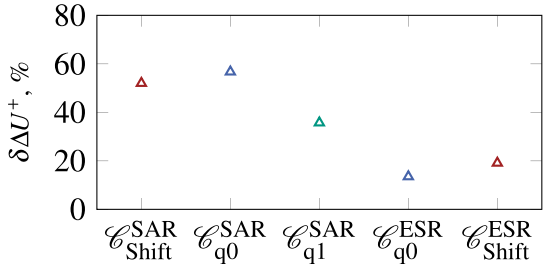

Fig. 7. Percentage variation of roughness function $\delta\Delta U^+$ of different types of surface anisotropy.

of ΔU^+ for $\mathscr{C}^{\text{SAR}}_{\text{q0},z}$ seems saturated when compared with $\mathscr{C}^{\text{SAR}}_{\text{shift},z}$, this could be attributed to the transition from the wavy regime toward the rough regime as evident in its ES_x value approaching 0.35 (Schultz and Flack, 2009). The observed difference in the variation of ΔU^+ across different types of anisotropy can be attributed to the distinct types of roughness anisotropy. Among the examined cases illustrated in Fig. 1, $\mathscr{C}_{\text{q1}}$ gradually converges toward the baseline isotropic state at smaller wavelengths. In contrast, $\mathscr{C}_{\text{q0}}$ displays a divergent behavior of PS at large wavenumbers, resulting in elongated small-scale structures. This disparity underscores that spanwise-aligned small-scale structures, namely $\mathscr{C}^{\text{SAR}}_{\text{q0},z}$, induce the highest drag. In contrast, for $\mathscr{C}^{\text{SAR}}_{\text{q1},z}$, more isotropic small-scale structures are expected. This distinction further explains the reversed drag ranking observed for streamwise roughness. Specifically, streamwise-aligned small-scale structures ($\mathscr{C}^{\text{SAR}}_{\text{q0},x}$) tend to produce lower drag compared to isotropic structures ($\mathscr{C}^{\text{SAR}}_{\text{q1},x}$), which exhibit less sensitivity to the flow direction.

Having recognized the limitations of SAR in accurately representing the surface anisotropy, the correlation between ΔU^+ and ESR is depicted in Fig. 4(b). It should be noted that the abscissa of this figure $ES_z/ES_x = 1/\text{ESR}$, which is adapted from the investigation in Jelly et al. (2022). Additionally, these anisotropic cases are connected with the reference case $\mathscr{C}_{\text{ref}}$, due to the fact that the entire database is generated based on the baseline 1-D PS. It can be seen from this figure that ΔU^+ undergoes more linear transitions, albeit with distinct slopes for each anisotropy type. Nevertheless, despite the observed trends, the scatter in ΔU^+ within the current characterization of surface anisotropy remains significant. This observation implies that these single-valued parameters may alone not fully encapsulate the multi-scale complexity of roughness, particularly in representing the varying effects of roughness anisotropy across different length scales.

The variation of ΔU^+ between spanwise-aligned roughness (ΔU^+_z) and streamwise-aligned roughness (ΔU^+_x) is expressed as $\delta\Delta U^+ = 100 \times \frac{\Delta U^+_z - \Delta U^+_x}{\Delta U^+_x}$ and depicted in Fig. 7 grouped by the type of surface anisotropy. It is evident that $\mathscr{C}^{\text{SAR}}_{\text{Shift}}$ and $\mathscr{C}^{\text{SAR}}_{\text{q0}}$ exhibit similar values of $\delta\Delta U^+ = 52\%$ and 57%, respectively, while $\delta\Delta U^+$ for $\mathscr{C}^{\text{ESR}}_{\text{shift}}$ and $\mathscr{C}^{\text{ESR}}_{\text{q0}}$ are notably lower with $\delta\Delta U^+ = 19\%$ and 14%, respectively. This suggests that the drag is more sensitive to the anisotropy in the range of small-scale roughness structures (corresponding to the structures at high wavenumbers). On the other hand, the cases with consistent ESR values, namely $\mathscr{C}^{\text{ESR}}_{\text{Shift}}$ and $\mathscr{C}^{\text{ESR}}_{\text{q0}}$, exhibit lower skin-friction difference which can be attributed to the significantly lower degree of anisotropy as reflected by their SAR values.

3.2. Impact of anisotropic roughness on heat transfer

The mean temperature profiles for the cases under consideration are presented in Fig. 8, using the same line styles as in Fig. 4. Evidently, The temperature profiles display noticeably less scatter compared to the velocity profiles, rendering an uncertainty in $\Delta\Theta^+$ ranging from −0.62 to +0.25 in viscous unit. Consistent with their influence on skin friction, spanwise-aligned roughness demonstrates a greater enhancement of heat transfer. The temperature roughness functions $\Delta\Theta^+$ along with St are documented in Table 1. In Fig. 9, $\Delta\Theta^+$ values are plotted against SAR and ESR. Interestingly, when comparing to their ΔU^+ counterpart, the evolution of $\Delta\Theta^+$ to the considered metrics is more intricate. This may be attributed to the absence of the pressure term in the energy equation, suggesting that the complexity of heat transfer on the surfaces extends to small-scale details of the roughness geometry. A narrower scatter is observed when plotted against 1/ESR, indicating the importance of ES in determining the surface anisotropy effect on temperature field. However, as the scatter suggests, a single-valued statistical parameter might still remain insufficient. Lastly, the impact of flow direction on the surface heat transfer is illustrated in Fig. 10. Interestingly, similar degree of the alteration of $\Delta\Theta^+$ is observed compared to ΔU^+. The variation of $\Delta\Theta^+$ ranges from $\delta\Delta\Theta^+ = 56.2\%$ to 12.0% for $\mathscr{C}^{\text{SAR}}_{\text{Shift}}$ and $\mathscr{C}^{\text{ESR}}_{\text{Shift}}$, respectively. It is evident that specific ranges of roughness wavelengths play a dominant role in influencing heat transfer modifications, depending on the orientation of the flow relative to these roughness structures.

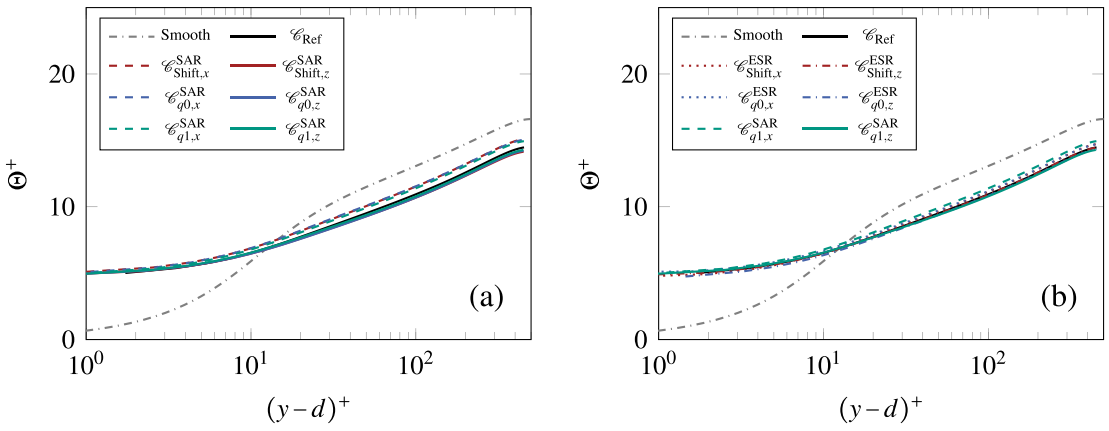

Fig. 8. DNS results of considered cases. The color indicates different types of roughness anisotropy. The inner-scaled mean temperature profiles are compared among the cases with same (a) SAR and (b) ESR.

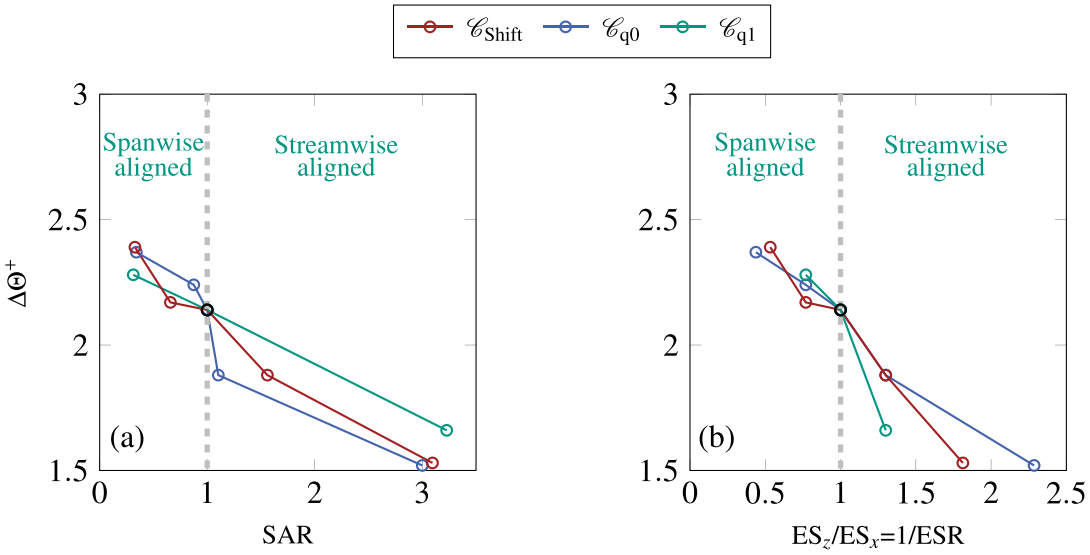

Fig. 9. The roughness function, $\Delta\Theta^+$, plotted as functions of the (a)SAR, (b) $\mathrm{ES}_z/\mathrm{ES}_x$ = 1/ESR. The color indicates different types of roughness anisotropy. The reference case $\mathscr{C}_{\mathrm{Ref}}$ is represented by black circle.

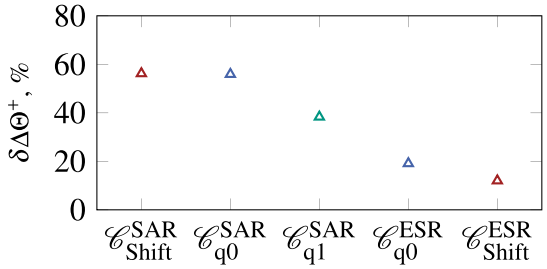

Fig. 10. Percentage variation of temperature roughness function $\delta\Delta\Theta^+$ of different types of surface anisotropy.

3.3. Secondary flow formation

To investigate the effect of introduced anisotropy on the formation of secondary motion an analysis of its intensity and flow topology is considered. For this purpose we evaluate the maximal secondary motion magnitude, given by $\left(\sqrt{V^2+W^2}/U_b\right)_{max}$, which represents the local peak velocity of the secondary flow. The magnitude is listed in the Table 1 for the considered roughness configurations. The presence of secondary motion is confirmed for the reference isotropic roughness case with a maximum magnitude of 2.3% of U_b, which is similar to the intensities reported for rough or heterogeneously rough surfaces (1-3% (Barros and Christensen, 2014; Stroh et al., 2020b)). Introduction of surface anisotropy resulting in streamwise aligned roughness structures does not significantly change the intensity of the secondary motion — for these surfaces the magnitude remains within the range of 2%–3% of U_b. For spanwise aligned roughness, a slightly stronger magnitude (>3%U_b) of the secondary motion is present with the highest magnitude of 3.5% U_b observed for $\mathscr{C}_{\mathrm{Shift}}$ and $\mathscr{C}_{q0}$ – anisotropic cases with elongated large-scale structures perpendicular to the flow direction (see Fig. 2b,d). This observation is in line with the behavior reported for heterogeneous roughness, where introduction of large-scale spanwise variation of roughness properties on the order of half channel height introduces a pronounced large-scale secondary motion (Jelly et al., 2022; Stroh et al., 2020b; Frohnapfel et al., 2024) – for the considered configurations the largest present roughness scale is $\lambda_0 = 2H$ (full channel height).

Fig. 11 shows an exemplary comparison of the mean velocity profile and the magnitude of secondary motion overlayed with the secondary motion streamlines in y-z-plane for the reference roughness $\mathscr{C}_{\mathrm{Ref}}$ and the streamwise/spanwise aligned anisotropic roughness $\mathscr{C}^{\mathrm{SAR}}_{\mathrm{Shift}}$. While the streamwise aligned version demonstrates a similar secondary motion magnitude compared to the reference case (maximum 2.1% vs.

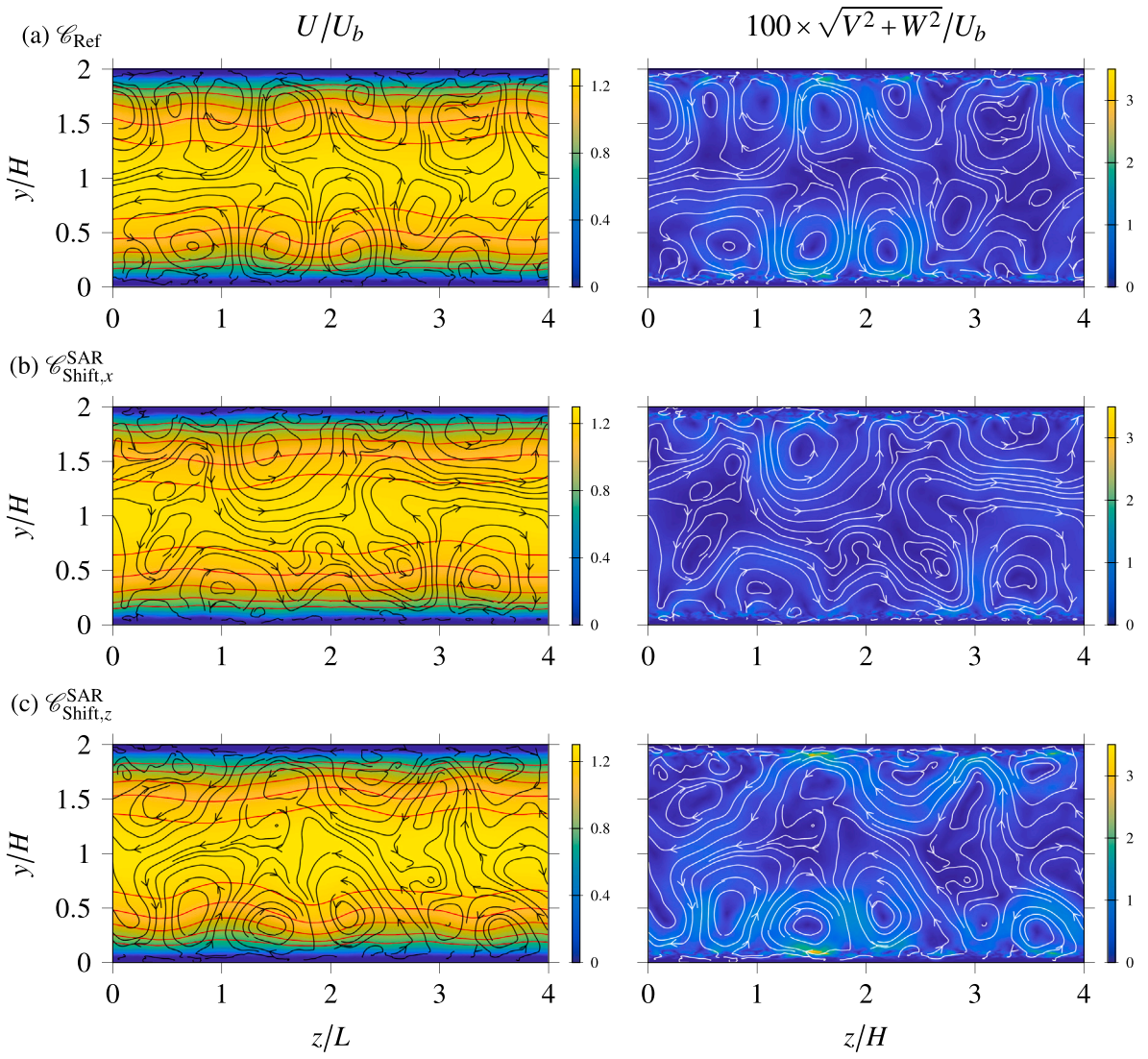

Fig. 11. Time–space-averaged velocity profile and magnitude of secondary motion for (a) $\mathscr{C}_{\mathrm{Ref}}$, (b) $\mathscr{C}^{\mathrm{SAR}}_{\mathrm{Shift},x}$ and (c) $\mathscr{C}^{\mathrm{SAR}}_{\mathrm{Shift},y}$. Black lines indicate time–space-averaged streamlines of secondary motion in the y–z-plane; red solid lines mark the isolines of the streamwise mean velocity distribution from 0.8 to 1.2 in 0.1 step.

2.3% U_b), the spanwise aligned version introduces a stronger secondary motion magnitude (maximum 3.2% U_b). For all considered cases a similar, predominantly large-scale secondary motion topology has been observed with a pronounced bulging of the mean velocity profile. The cases with lower secondary motion intensities (mostly streamwise aligned anisotropic roughness) tend to show more smaller scales in the secondary motion topology and to be less ordered than their higher-intensity counterpart (spanwise aligned anisotropic roughness). These observations might indicate a presence of secondary motion specific contribution to the enhanced momentum and heat transfer, which translates into additional dispersive stresses and heat fluxes (Stroh et al., 2020a). The analysis of those contributions is, however, out of the scope of the present study and can be assessed in the future work.

3.4. Characterization of surface anisotropy

Before an attempt to characterize the present anisotropic roughness, it is essential to discuss the topographical implications of the mentioned utilized parameters, namely SAR and ESR. As shown in Table 1, at a fixed SAR value, $\mathscr{C}^{\mathrm{SAR}}_{\mathrm{q1}}$ exhibits the ESR value closer to unity. Considering the convergence behavior of PS at high wavenumbers — as shown in Fig. 1(d), this implies that the ES, and thus the ESR, is predominantly influenced by small-scale roughness structures. In contrast, for cases where the ESR value is held constant, $\mathscr{C}^{\mathrm{ESR}}_{\mathrm{q0}}$ reveals a SAR value closer to unity. The gradual convergence of PS at low wavenumbers, as depicted in Fig. 1(c), suggests that L^{Corr}, and consequently the SAR parameter, is primarily governed by the contributions of larger-scale roughness structures.

Bearing this in mind, the significant scattering of ΔU^+ and $\Delta\Theta^+$ when plotted against SAR or ESR in Fig. 6 and 9 underscores the impact of anisotropy at various length scales on the resulting roughness skin friction. This serves as a motivation to explore new characterization parameters for roughness anisotropy by combining the two above parameters. Consequently, we propose a new parameter η_{SA} defined as

$$\eta_{\mathrm{SA}} = \frac{\mathrm{ESR}}{\mathrm{SAR}} = \frac{\langle\frac{\partial k}{\partial x}\rangle \times L_z^{Corr}}{\langle\frac{\partial k}{\partial z}\rangle \times L_x^{Corr}} \,. \tag{10}$$

The values of ΔU^+ and $\Delta\Theta^+$ for all investigated cases are plotted against η_{SA} in Figs. 12(a) and 13(a), respectively. The proposed parameter effectively captures anisotropic roughness by combining two scales: ESR, sensitive to small-scale surface variations, and SAR, reflecting larger-scale structure anisotropy. Together, ESR and SAR offer a comprehensive measure of scale-dependent anisotropy by encompassing both small- and large-scale effects on the turbulence. However, further

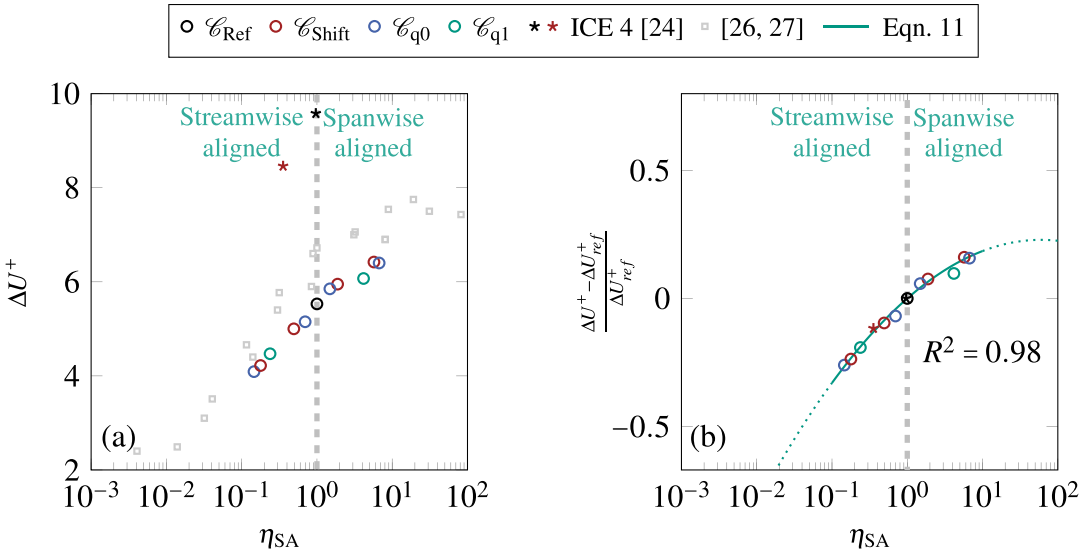

Fig. 12. The roughness function, ΔU^+, plotted against η_{SA} = ESR/SAR.

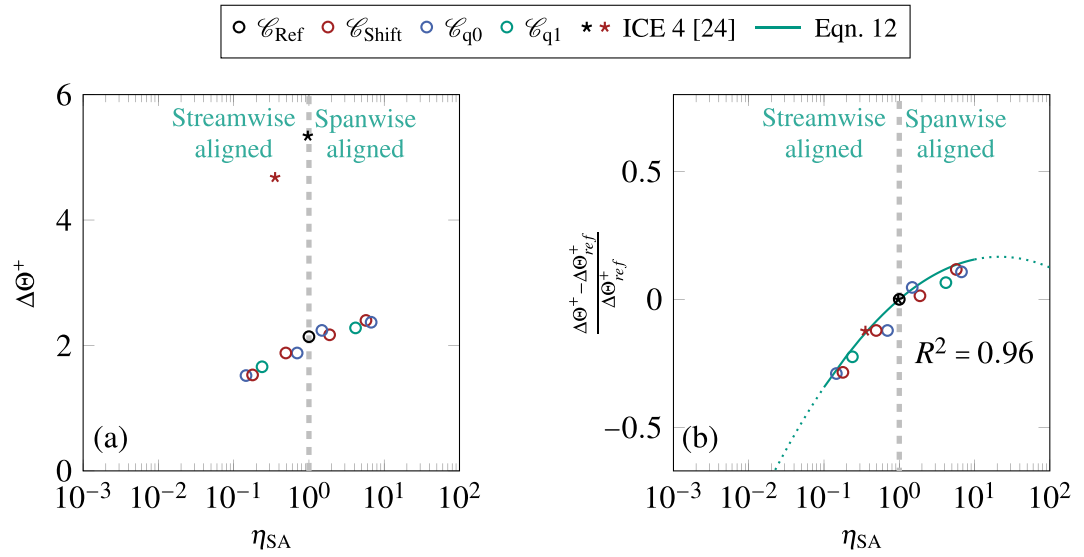

Fig. 13. The temperature roughness function, $\Delta\Theta^+$, plotted against ESR/SAR.

investigations with larger datasets are necessary to thoroughly understand and validate the underlying physical mechanisms represented by η_{SA}.

In Fig. 12(a), it is evident that the present data exhibit a clearly reduced scatter when plotted against η_{SA}, despite their varied forms of anisotropy. The anisotropic roughness data from previous studies (Jelly et al., 2022; Busse and Jelly, 2020) are shown with gray squares in Fig. 12(a). The incorporated data exhibit a consistent trend against η_{SA}. The scattering of ΔU^+ observed within the literature database can likely be attributed to variations in their baseline isotropic cases. Specifically, the data from the literature may not all be derived from the same baseline isotropic roughness configuration as employed in the present study. The influence of this variation on the hydrodynamic properties of the baseline isotropic roughness can be discerned from the scattering of ΔU^+ in Fig. 12(a) at $\eta_{\mathrm{SA}} \approx 1$. Having said that, it is obvious that the impact of spanwise aligned anisotropic roughness saturates at relatively high η_{SA} values, namely around 10~100. This is likely attributed to the suppression of streamwise flow channeling within the roughness canopy as the η_{SA} value increases, resulting in the formation of spanwise rod-like roughness structures. Based on this consideration, the alteration of roughness functions, compared to their isotropic baseline case $\Delta U^+_{\mathrm{Ref}}$, can be formulated with following correlation:

$$\frac{\Delta U^+ - \Delta U^+_{\mathrm{Ref}}}{\Delta U^+_{\mathrm{Ref}}} = 0.2575\log^2(\eta_{\mathrm{SA}}) - 0.0724\log(\eta_{\mathrm{SA}}) \,. \tag{11}$$

The constants are selected to provide the best fit of the data. The intercept constant is omitted with the aim of achieving $\Delta U^+ = \Delta U^+_{\mathrm{Ref}}$ for $\eta_{\mathrm{SA}} = 0$. The correlation function and the corresponding data are presented in Fig. 12(b). The current correlation achieves a coefficient of determination (R^2) of 0.98, demonstrating an excellent ability of Eq. (11) to capture the variations in the roughness function caused by surface anisotropy. To evaluate the present correlation, a realistic anisotropic roughness ICE4-R and its isotropic baseline roughness ICE4-A from the literature (Yang et al., 2023b) are included in Fig. 12. The red and black asterisks represent realistic and reference roughness, respectively. A notable difference in the roughness function is evident

in 12(a), resulting from variations in roughness parameters – such as height, skewness, or ES – compared to the present data set. Despite these differences, the impact of surface anisotropy of realistic roughness aligns remarkably well with the correlation as can be seen in Fig. 12(b).

The same roughness parameter is utilized to characterize the impact of roughness anisotropy on the temperature field. A minimal square fitting delivers the alteration of temperature roughness functions as:

$$\frac{\Delta\Theta^+ - \Delta\Theta^+_{\mathrm{Ref}}}{\Delta\Theta^+_{\mathrm{Ref}}} = 0.2497\log^2(\eta_{\mathrm{SA}}) - 0.0937\log(\eta_{\mathrm{SA}})\ . \tag{12}$$

The correlation function along with the data are illustrated in Fig. 13(b). A coefficient of determination R^2 of 0.96 is achieved. The realistic ice accretion anisotropic roughness along with its isotropic reference are included in Fig. 13, good collapse of the data is achieved by Eq. (12).

It is worth noting that this correlation is established within the range of the present dataset, namely with $0.1 \lesssim \eta_{\mathrm{SA}} \lesssim 10$ at $\mathrm{Re}_\tau = 500$, $Pr = 0.71$. The correlation functions within this range is represented by solid lines in Figs. 12 and 13. An extrapolation of this correlation (dashed lines) to broader span of surface anisotropy and as well as Re_τ and Pr requires further investigations in the future works and careful validations.

4. Conclusions

DNSs are performed to study skin friction and heat transfer coefficients of turbulent flow over irregular anisotropic roughness at $\mathrm{Re}_\tau = 500$ and $Pr = 0.71$ focusing on three types of surface anisotropy — denoted as $\mathscr{C}_{\mathrm{Shift}}$, $\mathscr{C}_{\mathrm{q0}}$, and $\mathscr{C}_{\mathrm{q1}}$. Each of these three types exhibit more pronounced anisotropic properties at a certain range of roughness scales. The studied surfaces are generated by adjusting the 2-D PS while either SAR or ESR is kept constant. Here SAR is defined as the ratio of streamwise to spanwise correlation lengths (L_x^{Corr}/L_z^{Corr}), while ESR is calculated as the ratio of streamwise to spanwise effective slopes ($\mathrm{ES}_x/\mathrm{ES}_z$). The effects of these anisotropic roughness structures are analyzed for both streamwise- and spanwise-aligned orientations. Their influence on skin friction is quantified as the percentage variation in the roughness function, $\delta\Delta U^+$, between the two alignment orientations for each roughness type. This variation is observed to range from 36% to 57% for roughness cases with fixed SAR values and from 14% to 36% for those with fixed ESR values. Similarly, comparable variations are observed in the variation of temperature roughness function, $\delta\Delta\Theta^+$, ranging from 38% to 56% and from 12% to 38% for roughness configurations with fixed SAR and ESR, respectively. Furthermore, it is found, that a secondary motion observed over reference isotropic roughness (maximum magnitude 2.3% of U_b) is barely affected by the streamwise aligned anisotropic roughness and slightly increased for spanwise aligned anisotropic roughness (maximum magnitude 3-3.5% of U_b).

Moreover, when we employed SAR and ESR for characterizing the effect of surface anisotropy on the resulting skin friction and heat transfer, a noticeable scatter is observed indicating that these parameters alone are insufficient to fully account for different types of roughness anisotropy. A new parameter $\eta_{\mathrm{SA}} = \mathrm{ESR}/\mathrm{SAR}$ is proposed in the present work, which is demonstrated to effectively reduce the scatter. Correlation functions capturing the anisotropic effects, based on the proposed parameter η_{SA}, are derived by fitting the present dataset. These functions achieve coefficients of determination R^2 of 0.98 and 0.96 for ΔU^+ and $\Delta\Theta^+$, respectively. Finally, the proposed correlations accurately predict the impact of surface anisotropy on the realistic roughness ICE 4 from the literature. However, it is important to note that the present study primarily focuses on a fixed roughness Reynolds number of $k^+ = 50$. While it ensures consistency within the dataset, it also locates the roughness on the border between transitionally rough and fully rough regimes. As such, the complexity of varying roughness behavior in the transitionally rough regime is not incorporated by the present work. Future studies should aim to extend the present framework to a broader range of Reynolds numbers to further investigate the roughness effect in the fully rough regime. Therefore, a potential topic for future research is to examine the influence of surface anisotropy on the equivalent sand grain size k_s. Additionally, the present observations on the temperature field are limited to $Pr = 0.71$. It is expected that with varying Prandtl numbers, the proposed temperature correlation (Eq. (12)) may require further modifications to account for the influence of the Prandtl number. Therefore, future research should extend the examination to a wider range of anisotropic rough surfaces as well as Prandtl numbers to assess its generalizability and to deepen the understanding of its physical implications.

CRediT authorship contribution statement

Jiasheng Yang: Writing – review & editing, Writing – original draft, Visualization, Validation, Methodology, Investigation, Formal analysis, Data curation, Conceptualization. **Alexander Stroh:** Writing – review & editing, Supervision, Project administration, Formal analysis, Conceptualization. **Shervin Bagheri:** Writing – review & editing, Supervision, Investigation, Formal analysis, Conceptualization. **Bettina Frohnapfel:** Writing – review & editing, Supervision, Resources, Formal analysis. **Pourya Forooghi:** Writing – review & editing, Supervision, Project administration, Methodology, Funding acquisition, Formal analysis, Conceptualization.

Declaration of competing interest

The authors declare the following financial interests/personal relationships which may be considered as potential competing interests: Jiasheng Yang reports financial support was provided by Karlsruhe Institute of Technology Karlsruhe House of Young Scientists. If there are other authors, they declare that they have no known competing financial interests or personal relationships that could have appeared to influence the work reported in this paper.

Acknowledgments

This work was performed on the supercomputer HoReKa and the storage facility LSDF funded by the Ministry of Science, Research and the Arts Baden-Württemberg, Germany and by the Federal Ministry of Education and Research, Germany. It was supported by the German Research Foundation (DFG) under the Collaborative Research Centre TRR150 (project number 237267381) and by the Karlsruhe House of Young Scientists (KHYS), Germany through a Research Travel Grant, which enabled J.Y.'s research stay at KTH Stockholm.

Data availability

Data will be made available on request.

References

Barros, Julio M., Christensen, Kenneth T., 2014. Observations of turbulent secondary flows in a rough-wall boundary layer. J. Fluid Mech. 748, R1.

Barros, J.M., Schultz, M.P., Flack, K.A., 2018. Measurements of skin-friction of systematically generated surface roughness. Int. J. Heat Fluid Flow 72, 1–7.

Busse, A., Jelly, T.O., 2020. Influence of surface anisotropy on turbulent flow over irregular roughness. Flow Turbul. Combust. 104, 331–354.

Busse, A., Thakkar, M., Sandham, N.D., 2017. Reynolds-number dependence of the near-wall flow over irregular rough surfaces. J. Fluid Mech. 810, 196–224.

Chan, L., MacDonald, M., Chung, D., Hutchins, N., Ooi, A., 2015. A systematic investigation of roughness height and wavelength in turbulent pipe flow in the transitionally rough regime. J. Fluid Mech. 771, 743–777.

Chevalier, M., Schlatter, P., Lundbladh, A., Henningson, D., 2007. SIMSON–a Pseudo-Spectral Solver for Incompressible Boundary Layer Flow. KTH, Stockholm, Sweden, pp. 1–100.

Chung, D., Hutchins, N., Schultz, M.P., Flack, K.A., 2021. Predicting the drag of rough surfaces. Annu. Rev. Fluid Mech. 53, 439–471.
Flack, K.A., 2018. Moving beyond moody. J. Fluid Mech. 842, 1–4.
Flack, K.A., Schultz, M.P., 2010. Review of hydraulic roughness scales in the fully rough regime. J. Fluids Eng. 132 (4).
Flack, K., Schultz, M., Barros, J., Kim, Y.C., 2016. Skin-friction behavior in the transitionally-rough regime. Int. J. Heat Fluid Flow 61, 21–30.
Forooghi, P., Stroh, A., Magagnato, F., Jakirlić, S., Frohnapfel, B., 2017. Toward a universal roughness correlation. J. Fluids Eng. 139 (12), 121201.
Frohnapfel, Bettina, von Deyn, Lars, Yang, Jiasheng, Neuhauser, Jonathan, Stroh, Alexander, Örlü, Ramis, Gatti, Davide, 2024. Flow resistance over heterogeneous roughness made of spanwise-alternating sandpaper strips. J. Fluid Mech. 980, A31.
Garg, H., Sahut, G., Tuneskog, E., Nogenmyr, C., Fureby, K., 2024. Large eddy simulations of flow over additively manufactured surfaces: Impact of roughness and skewness on turbulent heat transfer. Phys. Fluids 36 (8), 085143.
Goldstein, D., Handler, R., Sirovich, L., 1993. Modeling a no-slip flow boundary with an external force field. J. Comput. Phys. 105 (2), 354–366.
Hama, F.R., 1954. Boundary-layer characteristics for smooth and rough surfaces.
Holm M. P. Schultz, E.R., Bendick, J.A., Hertel, W.M., 2011. Economic impact of biofouling on a naval surface ship. Biofouling 27 (1), 87–98.
Jackson, P.S., 1981. On the displacement height in the logarithmic velocity profile. J. Fluid Mech. 111, 15–25.
Jelly, T.O., Ramani, A., Nugroho, B., Hutchins, N., Busse, A., 2022. Impact of spanwise effective slope upon rough-wall turbulent channel flow. J. Fluid Mech. 951, A1.
Jouybari, M.A., Yuan, J., Brereton, G.J., Murillo, M.S., 2021. Data-driven prediction of the equivalent sand-grain height in rough-wall turbulent flows. J. Fluid Mech. 912, A8.
Kader, B.A., 1981. Temperature and concentration profiles in fully turbulent boundary layers. Int. J. Heat Mass Transfer 24 (9), 1541–1544.
Kaminaris, Sotirios D., Womack, Kathryn M., Meneveau, Charles, Flack, Karen A., Schultz, Michael P., 2023. Secondary flows in turbulent boundary layers developing over truncated cone surfaces. J. Fluid Mech. 961, A23.
Kasagi, N., Tomita, Y., Kuroda, A., 1992. Direct numerical simulation of passive scalar field in a turbulent channel flow. J. Heat Transf. 114 (3), 598–606.
Kawamura, H., Abe, H., Matsuo, Y., 1999. Dns of turbulent heat transfer in channel flow with respect to reynolds and prandtl number effects. Int. J. Heat Fluid Flow 20 (3), 196–207.
MacDonald, M., Hutchins, N., Chung, D., 2019. Roughness effects in turbulent forced convection. J. Fluid Mech. 861, 138–162.
Medjnoun, Tarik, Napoli, Enrico, Demirel, Yigit Kemal, Atencio, Alexandra, Marchis, Mauro De, 2023. Assessment of aerodynamic roughness parameters of turbulent boundary layers over barnacle-covered surfaces. Exp. Fluids 64 (7), 169.
Nikuradse, J., 1933. Stroemungsgesetze in Rauhen Rohren. VDI-Verl., Berlin.
Peeters, J.W.R., Sandham, N.D., 2019. Turbulent heat transfer in channels with irregular roughness. Int. J. Heat Mass Transfer 138, 454–467.
Pérez-Ràfols, F., Almqvist, A., 2019. Generating randomly rough surfaces with given height probability distribution and power spectrum. Tribol. Int. 131, 591–604.
Ramani, A., Schilt, L., Nugroho, B., Busse, A., Jelly, T.O., Monty, J.P., Hutchins, N., 2024. An assessment of effective slope as a parameter for turbulent drag prediction over multi-scaled roughness. Exp. Fluids 65 (6), 78.
Raupach, M.R., 1992. Drag and drag partition on rough surfaces. Bound.-Layer Meteorol. 60, 375–395.
Sanhueza, R.D., Akkerman, I., Peeters, J.W.R., 2023. Machine learning for the prediction of the local skin friction factors and nusselt numbers in turbulent flows past rough surfaces. Int. J. Heat Fluid Flow 103, 109204.
Schultz, M.P., Flack, K.A., 2007. The rough-wall turbulent boundary layer from the hydraulically smooth to the fully rough regime. J. Fluid Mech. 580, 381–405.
Schultz, M.P., Flack, K.A., 2009. Turbulent boundary layers on a systematically varied rough wall. Phys. Fluids 21 (1), 015104.
Stroh, A., Schäfer, K., Forooghi, P., Frohnapfel, B., 2020a. Secondary flow and heat transfer in turbulent flow over streamwise ridges. Int. J. Heat Fluid Flow 81, 108518.
Stroh, A., Schäfer, K., Frohnapfel, B., Forooghi, P., 2020b. Rearrangement of secondary flow over spanwise heterogeneous roughness. J. Fluid Mech. 885, R5.
Thakkar, M., Busse, A., Sandham, N., 2017. Surface correlations of hydrodynamic drag for transitionally rough engineering surfaces. J. Turbul. 18 (2), 138–169.
Theobald, F., Schäfer, K., Yang, J., Frohnapfel, B., Stripf, M., Forooghi, P., Stroh, A., 2021. Comparison of different solvers and geometry representation strategies for dns of rough wall channel flow. In: WCCM-ECCOMAS 2020.
Townsend, A.A., 1976. The Structure of Turbulent Shear Flow / a.a.Townsend, second ed. Cambridge University Press Cambridge [Eng.], New York.
Vanderwel, C., Stroh, A., Kriegseis, J., Frohnapfel, B., Ganapathisubramani, B., 2019. The instantaneous structure of secondary flows in turbulent boundary layers. J. Fluid Mech. 862, 845–870.
Womack, Kathryn M., Kaminaris, Sotirios D., Ganju, Siddhartha, Meneveau, Charles, Schultz, Michael P., Flack, Karen A., 2022. Turbulent boundary layer flow over regularly and irregularly arranged truncated cone surfaces. J. Fluid Mech. 933, A2.
Yaglom, A.M., 1979. Similarity laws for constant-pressure and pressure-gradient turbulent wall flows. Annu. Rev. Fluid Mech. 11 (1), 505–540.
Yang, J., Stroh, A., Chung, D., Forooghi, P., 2022. Dns-based characterization of pseudo-random roughness in minimal channels. J. Fluid Mech. 941, A47.
Yang, J., Stroh, A., Jakirlic, S., Frohnapfel, B., Forooghi, P., 2021. Study of irregular roughness in minimal channels. In: ETMM 13, International Symposium on Engineering, Turbulence, Modelling and Measurement, 15.09.-17.09.2021.
Yang, J., Stroh, A., Lee, S., Bagheri, S., Frohnapfel, B., Forooghi, P., 2023a. Prediction of equivalent sand-grain size and identification of drag-relevant scales of roughness – a data-driven approach. J. Fluid Mech. 975, A34.
Yang, J., Velandia, J., Bansmer, A., Stroh, S., Forooghi, P., 2023b. A comparison of hydrodynamic and thermal properties of artificially generated against realistic rough surfaces. Int. J. Heat Fluid Flow 99, 109093.